Aalborg Universitet

A Simplified SISO Small-Signal Model for Analyzing Instability Mechanism of Grid-Forming Inverter under Stronger Grid

Huang, Liang; Wu, Chao; Zhou, Dao; Blaabjerg, Frede

A Simplified SISO Small-Signal Model for Analyzing Instability Mechanism of Grid-Forming Inverter under Stronger Grid

Liang Huang, Chao Wu, Dao Zhou, and Frede Blaabjerg
AAU Energy
Aalborg University
Aalborg East 9220, Denmark
lihu@energy.aau.dk, cwu@energy.aau.dk, zda@energy.aau.dk, fbl@energy.aau.dk

Abstract—**Different from grid-following inverters, grid-forming (GFM) inverters tend to be unstable under stronger grid conditions. However, the instability mechanism is still absent in existing research. To fill this gap, the full-order multiple-input multiple-output (MIMO) small-signal model of the GFM inverter is simplified as a single-input single-output (SISO) model on quadrature axis, so that the destabilizing factor can be clearly observed. Based on this SISO model, it is revealed that the power synchronization loop introducing an integral term into the voltage control loop is the main reason for instability. Decreasing the grid strength or the power droop gain can reduce the gain of the integral term and enhance stability. Finally, simulation and experimental results verify the effectiveness of theoretical analysis.**

Keywords—grid-forming inverter, simplified small-signal model, sub-synchronous oscillation, instability mechanism

I. INTRODUCTION

Nowadays, grid-following (GFL) inverters have been widely used in renewable energy generation systems, such as wind and solar photovoltaic (PV) power plants [1]. However, GFL inverters have some limitations to provide inertia support. Thus, the power system might suffer from frequency stability issues as the penetration of renewable energy sources increases and the total inertia decreases [2]. Moreover, the grid-following inverters behave like current sources, which rely on the grid voltage to realize synchronization and normal operation. Thus, the islanded operation is a big challenge for grid-following inverters [3].

Differently, grid-forming (GFM) inverters can support the grid frequency to solve the frequency stability issues. Two commonly used methods are virtual synchronous generator (VSG) control and droop control. When the virtual inertia is set as zero, the VSG control is equivalent to the droop control [4]. Moreover, grid-forming inverters behave like voltage sources so that they have the islanded operation ability. The islanded operation and frequency support are two obvious advantages of GFM inverters compared with GFL inverters. Therefore, GFM inverters have attracted a lot of attentions in recent years [5]-[8].

However, it is reported in [9] that conventional dual-loop GFM inverters tend to be unstable under stronger grid conditions. A duality theory is summarized in terms of GFM and GFL inverters, which shows that the voltage (current) source characteristic of the GFM (GFL) inverter makes it tend to be unstable in strong (weak) voltage-source grids [9]. Besides, it is reported in [10] that the instability behavior of GFM inverters in stronger grids is the sub-synchronous oscillation, where the resonant frequency is lower than the fundamental frequency (i.e. 50 Hz). Nevertheless, the instability mechanism of the sub-synchronous oscillation has not been illustrated clearly.

Considering that it is hard to analyze the stability of GFM inverter systems directly by using the nonlinear differential equations, the small-signal linearized model is an effective tool to analyze the stability of such nonlinear system around a fixed point [10]. Several small-signal models are introduced in [10]-[12] for stability analysis. The complex-valued small-signal impedance model in the *α-β* frame is used in [10]. Besides, the *d-q* small-signal state-space model and impedance model are used in [11] and [12]. Although these full-order small-signal models can predict the stability of the system, the reason for the instability cannot be intuitively observed because the full-order models are complicated.

In this paper, by properly simplifying the full-order multiple-input multiple-output (MIMO) small-signal model, a simplified single-input single-output (SISO) model is proposed, where the destabilizing factor can be clearly observed. Thus, an SISO open-loop transfer function can be calculated, and the Bode diagram can be used for stability analysis. From this SISO small-signal model, several conclusions can be summarized as below: 1) The power synchronization loop introducing an integral term into the voltage control loop is the reason for instability. 2) A stronger grid with a higher short-circuit ratio (SCR) leads to a higher gain of the integral term, which may worsen the stability. 3) Reducing the power droop gain can reduce the gain of the integral term and enhance stability.

The rest of this paper is organized as follows. Section II introduces the configurations of the typical GFM inverter with droop control. Then, its full-order MIMO small-signal model is established. In Section III, the full-order MIMO small-signal model is simplified as an SISO small-signal model by using some assumptions. In Section IV, the simulation and experimental results are provided to verify the theoretical analysis. Finally, this paper is concluded in Section V.

II. FULL-ORDER SMALL-SIGNAL MODEL OF GRID-FORMING INVERTER WITH DROOP CONTROL

A. Configuration of Typical Grid-Forming Inverter

Fig. 1 shows the configuration of the typical dual-loop GFM inverter with droop control. $V_c \angle \theta_c$ is the converter output voltage vector, $V_o \angle \theta_o$ is the output voltage vector at the point of common coupling (PCC) and $V_g \angle \theta_g$ is the grid voltage vector.
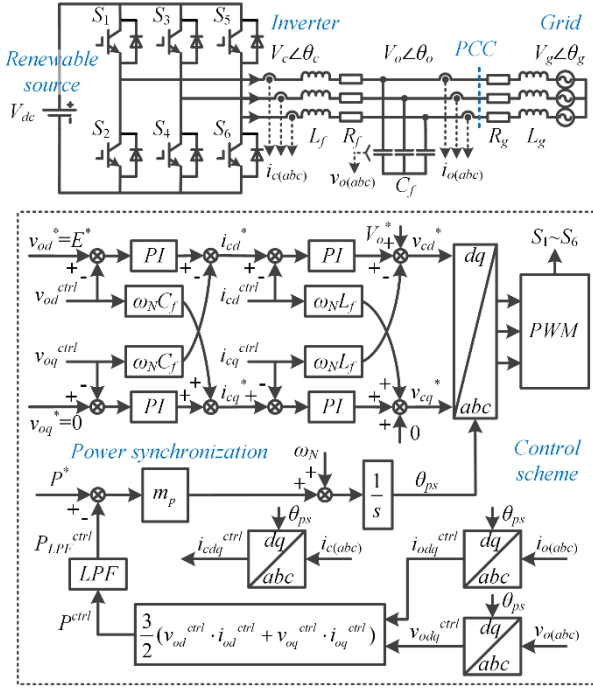
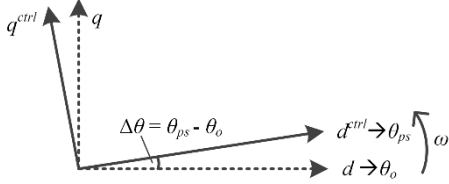Fig. 1.   Schematic of dual-loop grid-forming inverter with droop control.

Fig. 2.   Schematic of voltage-oriented rotating d-q frames.

The voltages $v_{o(abc)}$ are three-phase instantaneous output voltages at the PCC. The currents $i_{c(abc)}$ and $i_{o(abc)}$ are three-phase instantaneous converter currents and output currents at the PCC. The grid can be represented by a Thevenin equivalent impedance $Z_g = R_g + j\omega L_g$, where L_g and R_g are the equivalent grid inductance and resistance. The grid angular frequency ω is considered as a constant and equal to the nominal value ω_N. L_f and R_f are the output filter inductance and resistance. C_f is the output filter capacitance. To avoid much reactive power consumption on the capacitor, the value of C_f is designed relatively small. The control diagram includes a d-axis and q-axis inner current control loop, a d-axis and q-axis voltage control loop, and an outer active power droop control loop. The active power control loop is used for power synchronization. It should be pointed out that the reactive power droop control is omitted in this paper for simplifying analysis, so a constant reference $v_{od}{}^* = E^* = 1$ per unit (pu) is used for voltage control. The grid strength can be described by the SCR [13]. In this paper, a stronger grid condition with SCR=3 will be used to analyze the instability issues of the GFM inverter system.

The control system in Fig. 1 is performed in the rotating d-q frame, which is expected to oriented to the PCC voltage vector $V_o \angle \theta_o$. However, it is actually oriented to the angle θ_{ps} by using the power synchronization control. The angles θ_{ps} and θ_o are equal in the steady-state, but they have a small error in the dynamic state. Thus, the control d-q frame and the grid d-q frame are shown in Fig. 2. To be clear, the superscript '$ctrl$' denotes the variables in the control d-q frame in this paper.

B. Small-Signal Modeling

In order to analyze the stability of such a nonlinear system, small-signal models are effective tools. Since the small-signal impedance model with the modular structure can reflect the visualized relationship among variables [14], it is preferable to be used for stability analysis in this paper. In the following sections, the subscript '0' denotes a steady-state operating point, and the symbol 'Δ' denotes a small-signal perturbation of a variable.

The small-signal expressions of the physical circuits in the grid d-q frame are given by (1)-(3).

$$\begin{bmatrix} \Delta v_{od} \\ \Delta v_{oq} \end{bmatrix} - \begin{bmatrix} \Delta v_{gd} \\ \Delta v_{gq} \end{bmatrix} = \begin{bmatrix} sL_g + R_g & -\omega L_g \\ \omega L_g & sL_g + R_g \end{bmatrix} \cdot \begin{bmatrix} \Delta i_{od} \\ \Delta i_{oq} \end{bmatrix} \quad (1)$$

$$\begin{bmatrix} \Delta i_{cd} \\ \Delta i_{cq} \end{bmatrix} - \begin{bmatrix} \Delta i_{od} \\ \Delta i_{oq} \end{bmatrix} = \begin{bmatrix} sC_f & -\omega C_f \\ \omega C_f & sC_f \end{bmatrix} \cdot \begin{bmatrix} \Delta v_{od} \\ \Delta v_{oq} \end{bmatrix} \quad (2)$$

$$\begin{bmatrix} \Delta v_{cd} \\ \Delta v_{cq} \end{bmatrix} - \begin{bmatrix} \Delta v_{od} \\ \Delta v_{oq} \end{bmatrix} = \begin{bmatrix} sL_f + R_f & -\omega L_f \\ \omega L_f & sL_f + R_f \end{bmatrix} \cdot \begin{bmatrix} \Delta i_{cd} \\ \Delta i_{cq} \end{bmatrix} \quad (3)$$

where "s" represents the Laplace differential operator.

Besides, the small-signal expression of the inner current control loop is provided by (4).

$$\begin{bmatrix} \Delta v_{cd}{}^* \\ \Delta v_{cq}{}^* \end{bmatrix} = \begin{bmatrix} G_{pi\_I} & 0 \\ 0 & G_{pi\_I} \end{bmatrix} \cdot \left(\begin{bmatrix} \Delta i_{cd}{}^* \\ \Delta i_{cq}{}^* \end{bmatrix} - \begin{bmatrix} \Delta i_{cd}{}^{ctrl} \\ \Delta i_{cq}{}^{ctrl} \end{bmatrix} \right)$$
$$+ \begin{bmatrix} 0 & -\omega L_f \\ \omega L_f & 0 \end{bmatrix} \cdot \begin{bmatrix} \Delta i_{cd}{}^{ctrl} \\ \Delta i_{cq}{}^{ctrl} \end{bmatrix} \quad (4)$$

where $G_{pi\_I} = K_{p\_id} + K_{i\_id} / s = K_{p\_iq} + K_{i\_iq} / s$.

Similarly, the small-signal expression of the inner voltage control loop is shown as (5).

$$\begin{bmatrix} \Delta i_{cd}{}^* \\ \Delta i_{cq}{}^* \end{bmatrix} = \begin{bmatrix} G_{pi\_V} & 0 \\ 0 & G_{pi\_V} \end{bmatrix} \cdot \left(\begin{bmatrix} \Delta v_{od}{}^* \\ \Delta v_{oq}{}^* \end{bmatrix} - \begin{bmatrix} \Delta v_{od}{}^{ctrl} \\ \Delta v_{oq}{}^{ctrl} \end{bmatrix} \right)$$
$$+ \begin{bmatrix} 0 & -\omega C_f \\ \omega C_f & 0 \end{bmatrix} \cdot \begin{bmatrix} \Delta v_{od}{}^{ctrl} \\ \Delta v_{oq}{}^{ctrl} \end{bmatrix} \quad (5)$$

where $G_{pi\_V} = K_{p\_vd} + K_{i\_vd} / s = K_{p\_vq} + K_{i\_vq} / s$.

Moreover, the small-signal linearized expressions of the active power feedback and first-order low-pass filter (LPF) are shown as (6) and (7) respectively.

$$\Delta P^{ctrl} = \frac{3}{2} \begin{bmatrix} i_{od0} & i_{oq0} \end{bmatrix} \begin{bmatrix} \Delta v_{od}{}^{ctrl} \\ \Delta v_{oq}{}^{ctrl} \end{bmatrix} + \frac{3}{2} \begin{bmatrix} v_{od0} & v_{oq0} \end{bmatrix} \begin{bmatrix} \Delta i_{od}{}^{ctrl} \\ \Delta i_{oq}{}^{ctrl} \end{bmatrix} \quad (6)$$

$$\Delta P_{LPF}{}^{ctrl} = \frac{\omega_{LPF}}{s + \omega_{LPF}} \cdot \Delta P^{ctrl} = G_{LPF} \cdot \Delta P^{ctrl} \quad (7)$$

where ω_{LPF} is the cut-off angular frequency of the LPF.

In addition, the small-signal expression of the power synchronization control loop can be derived as (8).

$$\Delta \theta_{ps} = (\Delta P^* - \Delta P_{LPF}{}^{ctrl}) \cdot \frac{m_p}{s} \quad (8)$$
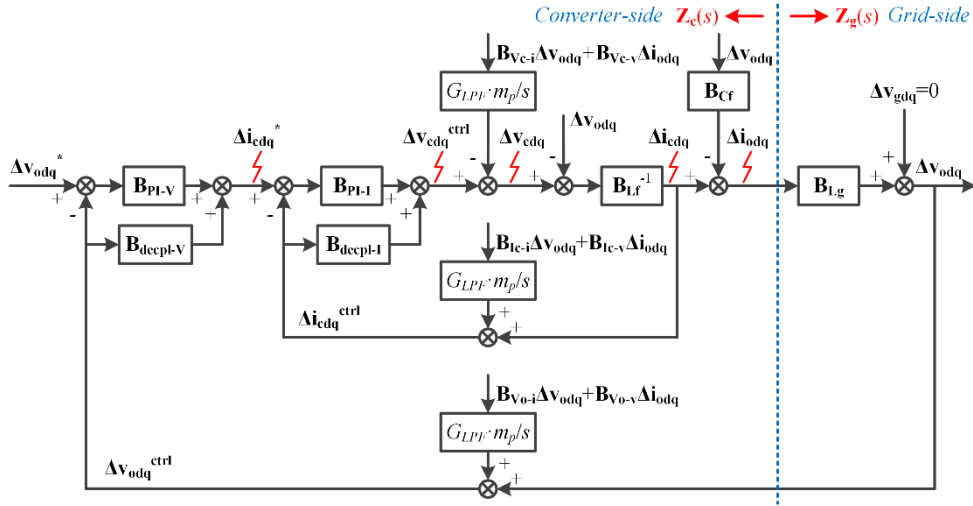
Fig. 3. Full-order small-signal impedance model of grid-forming inverter system.

$$\mathbf{Z_c}(s) = \{\mathbf{I} + \mathbf{B_{PI\text{-}I}}(\mathbf{B_{PI\text{-}V}} - \mathbf{B_{decpl\text{-}V}}) + (\mathbf{B_{Lf}} + \mathbf{B_{PI\text{-}I}} - \mathbf{B_{decpl\text{-}I}})\mathbf{B_{Cf}} + \frac{G_{LPF} m_p}{s} \cdot [\mathbf{B_{Vc\text{-}i}} + (\mathbf{B_{PI\text{-}I}} - \mathbf{B_{decpl\text{-}I}})\mathbf{B_{Ic\text{-}i}} + \mathbf{B_{PI\text{-}I}}(\mathbf{B_{PI\text{-}V}}$$

$$-\mathbf{B_{decpl\text{-}V}})\mathbf{B_{Vo\text{-}i}}]\}^{-1} \cdot \{(\mathbf{B_{Lf}} + \mathbf{B_{PI\text{-}I}} - \mathbf{B_{decpl\text{-}I}}) + \frac{G_{LPF} m_p}{s} \cdot [\mathbf{B_{Vc\text{-}v}} + (\mathbf{B_{PI\text{-}I}} - \mathbf{B_{decpl\text{-}I}})\mathbf{B_{Ic\text{-}v}} + \mathbf{B_{PI\text{-}I}}(\mathbf{B_{PI\text{-}V}} - \mathbf{B_{decpl\text{-}V}})\mathbf{B_{Vo\text{-}v}}]\}$$

(18)

Substituting (6) and (7) into (8), the expression of $\Delta\theta_{ps}$ can be derived as (9).

$$\Delta\theta_{ps} = [\Delta P^* - \frac{3}{2} \cdot G_{LPF} \cdot ([i_{od0} \quad i_{oq0}] \cdot \begin{bmatrix} \Delta v_{od}^{ctrl} \\ \Delta v_{oq}^{ctrl} \end{bmatrix}$$

$$+ [v_{od0} \quad v_{oq0}] \cdot \begin{bmatrix} \Delta i_{od}^{ctrl} \\ \Delta i_{oq}^{ctrl} \end{bmatrix})] \cdot \frac{m_p}{s}$$

(9)

The small-signal linearized expressions of the coordinate transformation between the grid d-q frame and the control d-q frame are given by (10)-(13).

$$\begin{bmatrix} \Delta v_{od}^{ctrl} \\ \Delta v_{oq}^{ctrl} \end{bmatrix} = \begin{bmatrix} \Delta v_{od} \\ \Delta v_{oq} \end{bmatrix} + \begin{bmatrix} v_{oq0} \\ -v_{od0} \end{bmatrix} \cdot \Delta\theta_{ps}$$

(10)

$$\begin{bmatrix} \Delta i_{od}^{ctrl} \\ \Delta i_{oq}^{ctrl} \end{bmatrix} = \begin{bmatrix} \Delta i_{od} \\ \Delta i_{oq} \end{bmatrix} + \begin{bmatrix} i_{oq0} \\ -i_{od0} \end{bmatrix} \cdot \Delta\theta_{ps}$$

(11)

$$\begin{bmatrix} \Delta i_{cd}^{ctrl} \\ \Delta i_{cq}^{ctrl} \end{bmatrix} = \begin{bmatrix} \Delta i_{cd} \\ \Delta i_{cq} \end{bmatrix} + \begin{bmatrix} i_{cq0} \\ -i_{cd0} \end{bmatrix} \cdot \Delta\theta_{ps}$$

(12)

$$\begin{bmatrix} \Delta v_{cd} \\ \Delta v_{cq} \end{bmatrix} = \begin{bmatrix} \Delta v_{cd}^{ctrl} \\ \Delta v_{cq}^{ctrl} \end{bmatrix} + \begin{bmatrix} -v_{cq0} \\ v_{cd0} \end{bmatrix} \cdot \Delta\theta_{ps}$$

(13)

Substituting (10) and (11) into (9), the expression of $\Delta\theta_{ps}$ can be derived as (14).

$$\Delta\theta_{ps} = [\Delta P^* - \frac{3}{2} \cdot G_{LPF} \cdot ([i_{od0} \quad i_{oq0}] \cdot \begin{bmatrix} \Delta v_{od} \\ \Delta v_{oq} \end{bmatrix}$$

$$+ [v_{od0} \quad v_{oq0}] \cdot \begin{bmatrix} \Delta i_{od} \\ \Delta i_{oq} \end{bmatrix})] \cdot \frac{m_p}{s}$$

(14)

Given $\Delta P^* = 0$, then substituting (14) into (10), (12) and (13), the expressions can be derived as (15)-(17).

$$\begin{bmatrix} \Delta v_{od}^{ctrl} \\ \Delta v_{oq}^{ctrl} \end{bmatrix} = \begin{bmatrix} \Delta v_{od} \\ \Delta v_{oq} \end{bmatrix} + (\begin{bmatrix} -v_{oq0}i_{od0} & -v_{oq0}i_{oq0} \\ v_{od0}i_{od0} & v_{od0}i_{oq0} \end{bmatrix} \cdot \begin{bmatrix} \Delta v_{od} \\ \Delta v_{oq} \end{bmatrix}$$

$$+ \begin{bmatrix} -v_{od0}v_{oq0} & -v_{oq0}^2 \\ v_{od0}^2 & v_{od0}v_{oq0} \end{bmatrix} \cdot \begin{bmatrix} \Delta i_{od} \\ \Delta i_{oq} \end{bmatrix}) \cdot \frac{3}{2} \cdot G_{LPF} \cdot \frac{m_p}{s}$$

(15)

$$\begin{bmatrix} \Delta i_{cd}^{ctrl} \\ \Delta i_{cq}^{ctrl} \end{bmatrix} = \begin{bmatrix} \Delta i_{cd} \\ \Delta i_{cq} \end{bmatrix} + (\begin{bmatrix} -i_{cq0}i_{od0} & -i_{cq0}i_{oq0} \\ i_{cd0}i_{od0} & i_{cd0}i_{oq0} \end{bmatrix} \cdot \begin{bmatrix} \Delta v_{od} \\ \Delta v_{oq} \end{bmatrix}$$

$$+ \begin{bmatrix} -i_{cq0}v_{od0} & -i_{cq0}v_{oq0} \\ i_{cd0}v_{od0} & i_{cd0}v_{oq0} \end{bmatrix} \cdot \begin{bmatrix} \Delta i_{od} \\ \Delta i_{oq} \end{bmatrix}) \cdot \frac{3}{2} \cdot G_{LPF} \cdot \frac{m_p}{s}$$

(16)

$$\begin{bmatrix} \Delta v_{cd} \\ \Delta v_{cq} \end{bmatrix} = \begin{bmatrix} \Delta v_{cd}^{ctrl} \\ \Delta v_{cq}^{ctrl} \end{bmatrix} - (\begin{bmatrix} -v_{cq0}i_{od0} & -v_{cq0}i_{oq0} \\ v_{cd0}i_{od0} & v_{cd0}i_{oq0} \end{bmatrix} \cdot \begin{bmatrix} \Delta v_{od} \\ \Delta v_{oq} \end{bmatrix}$$

$$+ \begin{bmatrix} -v_{cq0}v_{od0} & -v_{cq0}v_{oq0} \\ v_{cd0}v_{od0} & v_{cd0}v_{oq0} \end{bmatrix} \cdot \begin{bmatrix} \Delta i_{od} \\ \Delta i_{oq} \end{bmatrix}) \cdot \frac{3}{2} \cdot G_{LPF} \cdot \frac{m_p}{s}$$

(17)

Overall, the 2×2 matrixes in (1)-(5) and (15)-(17) can be represented by symbols $\mathbf{B_{Lg}}$, $\mathbf{B_{Cf}}$, $\mathbf{B_{Lf}}$, $\mathbf{B_{PI\text{-}I}}$, $\mathbf{B_{decpl\text{-}I}}$, $\mathbf{B_{PI\text{-}V}}$, $\mathbf{B_{decpl\text{-}V}}$, $\mathbf{B_{Vo\text{-}i}}$, $\mathbf{B_{Vo\text{-}v}}$, $\mathbf{B_{Ic\text{-}i}}$, $\mathbf{B_{Ic\text{-}v}}$, $\mathbf{B_{Vc\text{-}i}}$ and $\mathbf{B_{Vc\text{-}v}}$. Thus, the full-order small-signal model of the GFM inverter system in Fig. 1 is shown in Fig. 3, where $\mathbf{Z_c}(s)$ and $\mathbf{Z_g}(s)$ are the equivalent impedances on the converter-side and grid-side.

According to the small-signal control structure in Fig. 3, $\mathbf{Z_c}(s)$ and $\mathbf{Z_g}(s)$ can be derived as (18) and (19).

$$\mathbf{Z_g}(s) = \mathbf{B_{Lg}}$$

(19)

The control parameters can be designed as follows. Take $G_{pi\_I} = \omega_i L_f + \omega_i R_f / s$ and $G_{pi\_V} = \omega_v C_f + \omega_v / R_{po} / s$, where a pre-set output resistor R_{po} equal to 10 Ω is used for designing PI parameters of the voltage control loop.

According to (18) and (19), the matrix $\mathbf{Z_c}(s) \cdot \mathbf{Z_g}(s)^{-1}$ can be used for the generalized Nyquist criterion (GNC) to analyze the stability of the system [10].

TABLE I. PARAMETERS OF GRID-FORMING INVERTER SYSTEM

| Parameters	Values
Grid phase voltage (peak value), V_g	50 V
Grid frequency, f_g	50 Hz
Rated power of inverter, S_N	800 VA
Maximum current of inverter (peak value), I_{max}	10.7 A
DC-link voltage, V_{dc}	700 V
Output filter inductor, L_f	5 mH
Output filter capacitor, C_f	10 μF
R/X ratio of grid impedance, R_g/X_g	0.01
Short circuit ratio, SCR	1, 2, 3
Grid inductor, L_g	15.3, 10.2, 5.1 mH
Grid resistor, R_g	48, 32, 16 mΩ
Switching/sampling frequency, f_s	10 kHz
Designed current-loop bandwidth, ω_i	4000 rad/s
Designed voltage-loop bandwidth, ω_v	800 rad/s
Active power droop coefficient, m_p	5% ω_0/P_0
Cut-off angular frequency of LPF, ω_{LPF}	60 rad/s
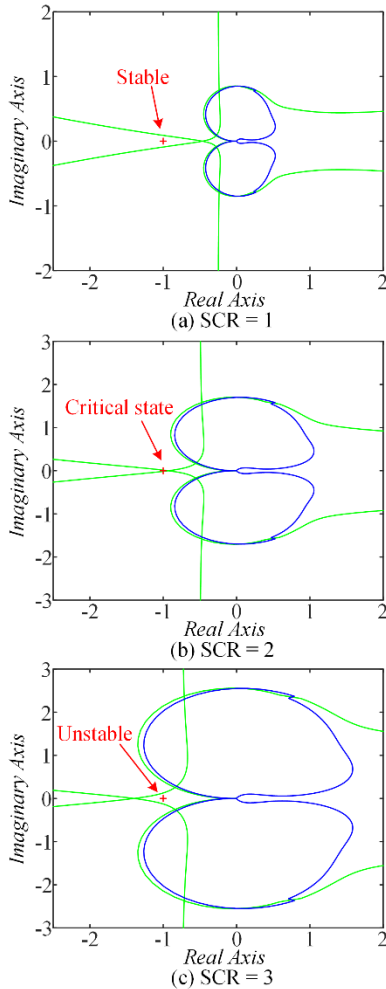
Fig. 4. Generalized Nyquist diagrams of full-order small-signal impedance model with different SCRs.

According to the steady-state equations, the steady-state operating points can be derived as: $v_{od0} = V_o = E^*$, $v_{oq0} = 0$, $i_{cd0} = i_{od0}$, $i_{cq0} = i_{oq0} + \omega C_f V_o$, $v_{cd0} = v_{od0} + R_f i_{cd0} - \omega L_f i_{cq0}$, and $v_{cq0} = v_{oq0} + R_f i_{cq0} + \omega L_f i_{cd0}$.

Based on the generalized Nyquist stability analyses of $\mathbf{Z_c}(s) \cdot \mathbf{Z_g}(s)^{-1}$ and parameters sensitivity analyses, it is found that the unstable states of the GFM inverter have weak relationship with the power. Hence, the zero power condition is used for simplifying analysis. Thus, the steady-state operating points can be given as: $i_{od0} = 0$, $i_{oq0} = 0$, $i_{cd0} = 0$, $i_{cq0} = \omega C_f V_o$, $v_{cd0} = V_o - \omega L_f \cdot \omega C_f V_o$, and $v_{cq0} = R_f \cdot \omega C_f V_o$.

The parameters of an 800 W dual-loop GFM inverter with droop control are shown in Table I, which is used as an example for stability analyses in this paper. Based on the matrix $\mathbf{Z_c}(s) \cdot \mathbf{Z_g}(s)^{-1}$, the generalized Nyquist diagrams with different SCRs are shown in Fig. 4. It can be seen that as the SCR increases, the stability of the system is getting worse. The system is unstable under a stronger grid condition (SCR ≥ 3). However, the reason for instability cannot be intuitively observed from the full-order small-signal model due to its complexity. In the next section, the model will be simplified.

III. SIMPLIFIED SMALL-SIGNAL MODEL

As analyzed in the previous section, the unstable states of GFM inverter still exist under the zero power conditions. Given $i_{od0} = 0$ and $i_{oq0} = 0$, thus, $\mathbf{B_{Vc-i}}$, $\mathbf{B_{Ic-i}}$, $\mathbf{B_{Vo-i}}$ are equal to $\mathbf{0}$. Since C_f is very small, assuming that $i_{cq0} = \omega C_f V_o \approx 0$, so $\mathbf{B_{Ic-v}} \approx \mathbf{0}$. Then, the small-signal model in Fig. 3 can be simplified as Fig. 5(a).

Furthermore, due to high bandwidth of the inner current loop, the disturbance term after the current PI controller can be ignored. Thus, the current loop is assumed as 1. Then, the small-signal model in Fig. 5(a) can be simplified as Fig. 5(b).

Based on Fig. 5(b), it can be found that the d-d channel element in the matrix ($\mathbf{B_{Vo-v}} \cdot \mathbf{B_{Lg}}^{-1}$) on the feedback loop is 0. Hence, the q-q channel should be responsible for instability. A similar assumption is used in [15] for analyzing GFL inverters. Thus, only considering the q-q channel and ignoring the dynamic of L_g, Fig. 5(b) can be simplified as Fig. 5(c).
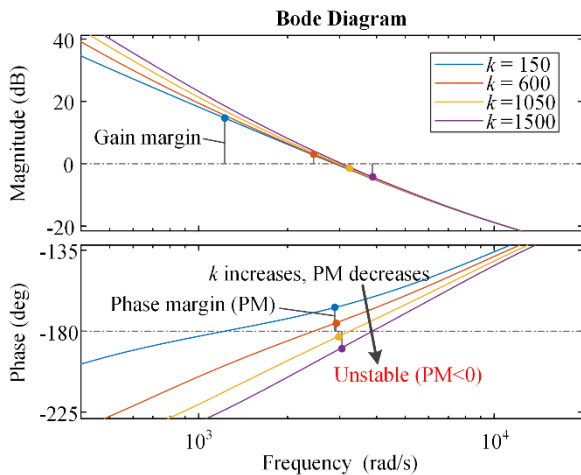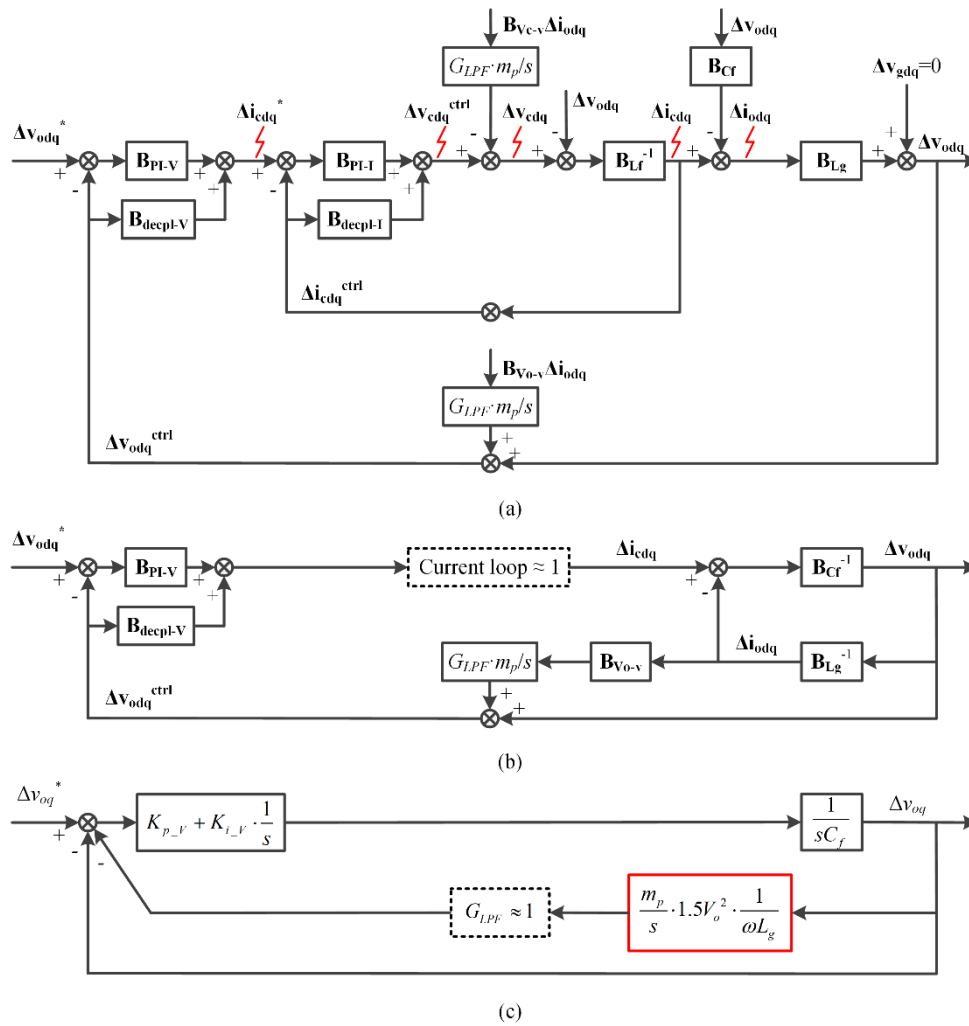
In addition, assuming that the LPF is equal to 1, then the open-loop transfer function $T_{ol}(s)$ of the SISO model in Fig. 5(c) can be derived as (20).

$$T_{ol}(s) = (K_{p\_V} + \frac{K_{i\_V}}{s}) \cdot \frac{1}{sC_f} \cdot (1 + \frac{k}{s}) \qquad (20)$$
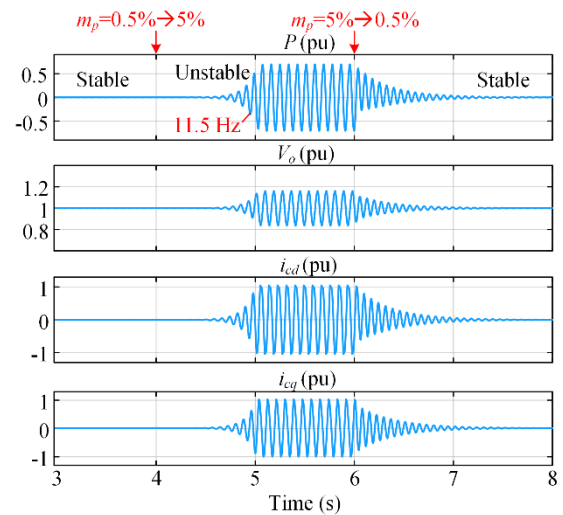
where $k = m_p \cdot 1.5 V_o^2/(\omega L_g)$ is the gain of the integral term.

The Bode diagram of $T_{ol}(s)$ is shown in Fig. 6. It can be seen that as k increases, the phase margin is reduced. When the phase margin is smaller than 0, the system is unstable. Therefore, the integral term k/s in (20) is the main reason for instability. Thus, when the SCR increases, the grid inductance L_g decreases and it leads to a larger k, which might worsen stability. Inversely, reducing the power droop gain m_p can reduce k and enhance stability.

However, reducing m_p is not the optimal solution, because m_p cannot be designed too small. Besides, under the super strong grid condition ($L_g = 0$), reducing m_p is not effective, because the gain k is infinite. Thus, it is necessary to find better solutions to enhance stability of the GFM inverter under strong grid conditions, which needs further study.

Fig. 5. Simplified small-signal model.

Fig. 6. Bode diagram of open-loop transfer function $T_{ol}(s)$.

Fig. 7. Simulation results with SCR=3.

IV. SIMULATION AND EXPERIMENTAL RESULTS

In order to verify the correctness of the analysis above, a GFM inverter simulation model is established in Matlab/Simulink, where the parameters in Table I are used. The simulation results with SCR=3 are shown in Fig. 7.

As shown in Fig. 7, when the power droop gain m_p is increased from 0.5% to 5% at the moment of 4s, the system becomes unstable. However, when m_p is decreased to 0.5% at the instant of 6s, the system becomes stable again. These simulation results reflect that increasing m_p can worsen the stability, which agrees with the theoretical analysis in Fig. 6.
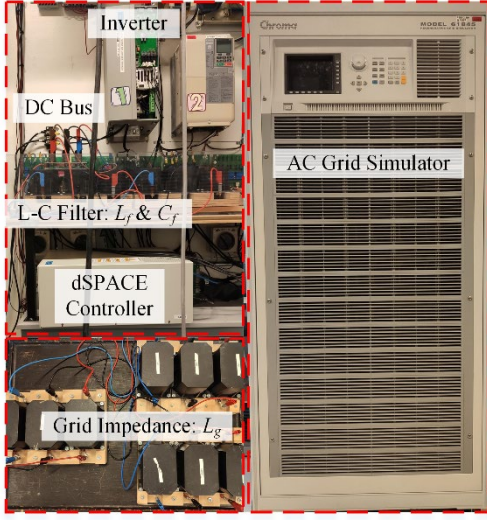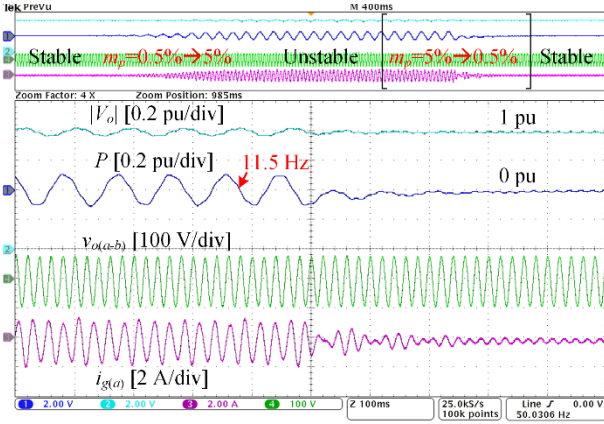
Fig. 8.   Photo of experimental setup.

Fig. 9.   Experimental results with SCR=3.

V. Conclusion

A simplified SISO small-signal model of the typical dual-loop GFM inverter with droop control is proposed in this paper. Based on this SISO model, it is revealed that the power synchronization loop introducing an integral term into the voltage control loop is the reason for instability. A stronger grid with a higher SCR leads to a higher gain of the integral term, which might worsen the stability. Reducing the power droop gain can reduce the gain of the integral term and enhance stability. However, when the grid strength is very high, reducing power droop gain is not an effective way. It is necessary to find better solutions to address this problem, which will be follow-up work in the future.

To verify the above analysis, the experimental tests are carried out on an 800 W GFM inverter. The experimental setup is shown in Fig. 8. The infinite grid is realized by using a grid simulator Chroma 61845. The grid-connected inverter is implemented by using the Danfoss FC 103P11KT11, and the control algorithms are implemented through the device dSPACE1007. The experimental results with SCR=3 are shown in Fig. 9, where the parameters in Table I are used for experiments.

As shown in Fig. 9, the system is stable initially. When the power droop gain m_p is increased from 0.5% to 5%, the system becomes unstable. Then, when m_p is decreased from 5% to 0.5%, the system becomes stable again. The sub-synchronous oscillation at 11.5 Hz can be observed during the unstable period. These experimental results agree with the simulation results in Fig. 7.

It is worth mentioning that the accuracy of the small-signal model is reduced during the simplifying process, which means that the simplified SISO model cannot take place of the full-order MIMO model for the quantitative analysis. Therefore, this paper provides a qualitative analysis by using the simplified SISO model. Although the accuracy of the simplified model is lower than that of the full-order model, it provides an intuitive view to observe the main destabilizing factor of the GFM inverter system.

References

[1] L. Huang, C. Wu, D. Zhou, and F. Blaabjerg, "A double-PLLs-based impedance reshaping method for extending the stability range of grid-following inverter under weak grid," *IEEE Trans. Power Electron.*, 2021, conditional acceptance.

[2] J. Matevosyan, B. Badrzadeh, T. Prevost, E. Quitmann, D. Ramasubramanian, et al., "Grid-forming inverters: Are they the key for high renewable penetration?," *IEEE Power Energy Mag.*, vol. 17, no. 6, pp. 89-98, Nov.-Dec. 2019.

[3] J. Rocabert, A. Luna, F. Blaabjerg and P. Rodríguez, "Control of power converters in AC microgrids," *IEEE Trans. Power Electron.*, vol. 27, no. 11, pp. 4734-4749, Nov. 2012.

[4] D. Pan, X. Wang, F. Liu and R. Shi, "Transient stability of voltage-source converters with grid-forming control: A design-oriented study," *IEEE J. Emerg. Sel. Top. Power Electron.*, vol. 8, no. 2, pp. 1019-1033, Jun. 2020.

[5] R. Rosso, X. Wang, M. Liserre, X. Lu and S. Engelken, "Grid-forming converters: control approaches, grid-synchronization, and future trends - A review," *IEEE Open J. Ind. Appl.*, vol. 2, pp. 93-109, 2021.

[6] K. De Brabandere, B. Bolsens, J. Van den Keybus, A. Woyte, J. Driesen and R. Belmans, "A voltage and frequency droop control method for parallel inverters," *IEEE Trans. Power Electron.*, vol. 22, no. 4, pp. 1107-1115, Jul. 2007.

[7] S. D'Arco and J. A. Suul, "Virtual synchronous machines - classification of implementations and analysis of equivalence to droop controllers for microgrids," *IEEE Gren. Conf.*, pp. 1-7, 2013.

[8] P. Mitra, L. Zhang and L. Harnefors, "Offshore wind integration to a weak grid by VSC-HVDC links using power-synchronization control: A case study," *IEEE Trans. Power Del.*, vol. 29, no. 1, pp. 453-461, Feb. 2014.

[9] Y. Li, Y. Gu, and T. C. Green, "Rethinking grid-forming and grid-following inverters: A duality theory," *arXiv:2105.13094 (preprint)*, pp. 1-9, 2021.

[10] Y. Liao, X. Wang, F. Liu, K. Xin and Y. Liu, "Sub-synchronous control interaction in grid-forming VSCs with droop control," *IEEE Work. Electron. Grid (eGrid)*, pp. 1-6, 2019.

[11] K. Yu, Q. Ai, S. Wang, J. Ni and T. Lv, "Analysis and optimization of droop controller for microgrid system based on small-signal dynamic model," *IEEE Trans. Smart Grid*, vol. 7, no. 2, pp. 695-705, Mar. 2016.

[12] S. Wang, Z. Liu, J. Liu, D. Boroyevich and R. Burgos, "Small-signal modeling and stability prediction of parallel droop-controlled inverters based on terminal characteristics of individual inverters," *IEEE Trans. Power Electron.*, vol. 35, no. 1, pp. 1045-1063, Jan. 2020.

[13] L. Huang, C. Wu, D. Zhou, and F. Blaabjerg, "Impact of grid strength and impedance characteristics on the maximum power transfer capability of grid-connected inverters," *Appl. Sci.*, vol. 11, no. 9, p. 4288, May 2021.

[14] L. Huang, C. Wu, D. Zhou, and F. Blaabjerg, "Comparison of three small-signal stability analysis methods for grid-following inverter," *Int. Conf. Opt. Electr. Electron. Equip. (OPTIM)*, 2021, in press.

[15] J. Fang, X. Li, H. Li and Y. Tang, "Stability improvement for three-phase grid-connected converters through impedance reshaping in quadrature-axis," *IEEE Trans. Power Electron.*, vol. 33, no. 10, pp. 8365-8375, Oct. 2018.